Università di Pisa

Two-dimensional modeling of etched strained-silicon quantum wires

Gilberto Curatola
Dipartimento di Ingegneria dell'Informazione: Elettronica, Informatica, Telecomunicazioni,
Università di Pisa
Giuseppe Iannaccone
Dipartimento di Ingegneria dell'Informazione: Elettronica, Informatica, Telecomunicazioni,
Università di Pisa

G. Curatola, G. Iannaccone, *Two-dimensional modeling of etched strained-silicon quantum wires*, Journal of Applied Physics, **95**, pp.1251-1257 (2004).

HTML ABSTRACT + LINKS

JOURNAL OF APPLIED PHYSICS VOLUME 95, NUMBER 3 1 FEBRUARY 2004

Two-dimensional modeling of etched strained-silicon quantum wires

G. Curatola[a] and G. Iannaccone[b]
Dipartimento di Ingegneria dell'Informazione, Università degli studi di Pisa, Via Diotisalvi 2, I-56122 Pisa, Italy

(Received 3 March 2003; accepted 7 November 2003)

We present two-dimensional simulations of different types of strained-silicon quantum wires obtained by selective etching on silicon germanium heterostructures. Such structures are promising both for emerging ballistic devices in silicon compatible technology and for innovative nanoscale field-effect transistors. Numerical modeling has been performed with a procedure designed to solve the Poisson–Schrödinger equation for electrons and holes, that takes into account the effect of strain on the band structure, conduction band anisotropy, and the effect of states at the exposed surfaces. We show that the simulations provide insights into the capability to control the wire via an external gate voltage, and into the dependence of wire properties on geometry and surface states. © *2004 American Institute of Physics*. [DOI: 10.1063/1.1637141]

I. INTRODUCTION

Progress in strained-silicon (SS) technology is enabling researchers to investigate, in silicon germanium heterostructures, mesoscopic transport phenomena typically observed in III–V material systems. This effort is justified mainly by the compatibility of SS with complementary metal oxide semiconductor (CMOS) technology, which is particularly important if device applications of transport in strongly confined systems are pursued.

Electron mobility up to 2830 cm^{-2}/Vs at 300 K[1] and up to 8×10^5 cm^{-2}/Vs at 15 K[2] has been obtained in SS quantum wells, due mainly to improvements in the growth of defect-free, virtual silicon–germanium substrates. The material itself is quite promising: tensile strain causes a splitting of the sixfold degenerate conduction band (CB) into twofold and fourfold degenerate valleys, and hence leads to a preferential occupation of CB minima and to reduced intervalley scattering. Under such circumstances, it is therefore possible to fabricate mesoscopic devices operating in the ballistic transport regime. For the same reason, SS is an extremely important material from an industrial point of view, and is being introduced in latest CMOS technology generations to improve high-frequency operation and reduce power dissipation.[3]

Very recently, Wieser *et al.*[4] demonstrated ballistic transport at 4.2 K in a quantum point contact realized on a modulation-doped $Si/Si_{0.7}Ge_{0.3}$ heterostructure, measuring quantization of conductance in multiples of $4q^2/h$, where the factor 4 is due to valley and spin degeneracy, q is the elementary charge, and h is Planck's constant.

From the point of view of basic physics, etched quantum wires (QWs) are extremely promising for obtaining the large subband splitting required to suppress intersubband scattering and achieve conductance quantization in very long wires, as has been possible in the III–V material system.[5–7]

However, etched QWs are also very promising for applications in alternative ballistic devices,[8] and as innovative structures for metal oxide semiconductor field-effect transistors (MOSFETs). As far as this last point is concerned, devices consisting of several etched QWs in parallel with double or triple gates have been recently proposed to suppress short-channel effects in nanoscale MOSFETs.[9] In addition, the well-known fin field-effect transistors can be seen as consisting of several wires in parallel with triple gates.[10,11]

In this article, we focus on the simulation of the electrical properties of strongly confined SSQWs obtained by selective etching on silicon germanium heterostructures controlled via an external gate. We consider two main structures: a QW with a triple metal gate, and a QW controlled by etched side gates.

Such structures comprise a large fraction of Si and SiGe wires considered in the literature, including both alternative FET structures and more "exotic" mesoscopic devices. Let us point out that, in addition to the structure described in Ref. 4, other etched silicon germanium QWs have been fabricated and characterized at cryogenic temperatures,[12–14] but only the one described in Ref. 12 exhibited conductance quantization. A much broader range of experiments has been performed on etched QWs in the AlGaAs/GaAs material system, showing extremely interesting transport properties and device applications (e.g., Ref. 8), that would be even more promising if transferred to the CMOS-compatible Si/SiGe material system.

From the simulation point of view, SS poses some additional problems with respect to AlGaAs–GaAs: the effect of strain on the band structure has to be fully included, as well as anisotropy and multiple minima in silicon CB, and strain-induced anisotropy in silicon valence band (VB).

The paper is organized as follows: In Sec. II, we illustrate the model used in the simulation; in Sec. III, we describe the two etched structures considered, and in Sec. IV, the main results obtained. The Conclusion section ends the paper. Appendix A describes the method used to take into account the effect of strain in silicon and silicon germanium.

[a]Electronic mail: g.curatola@iet.unipi.it
[b]Electronic mail: g.iannaccone@iet.unipi.it

 © 2004 American Institute of Physics

Downloaded 13 Jun 2007 to 131.114.53.157. Redistribution subject to AIP license or copyright, see http://jap.aip.org/jap/copyright.jsp

II. MODEL

Quantum confinement and charge distribution in QWs is investigated by solving the Schrödinger–Poisson equation in two dimensions with density functional theory. The nonlinear Poisson equation for the electrostatic potential Φ is

$$\nabla\cdot(\epsilon\nabla\Phi)=-\rho(\mathbf{r})=-q[-n(\mathbf{r})+p(\mathbf{r})+N_D^+(\mathbf{r})-N_A^-(\mathbf{r})], \tag{1}$$

where ϵ is the dielectric constant, n and p the electron and hole concentrations, respectively, and N_D^+ and N_A^- the ionized donor and acceptor concentrations respectively.[15] Equation (1) is discretized with box integration on a nonuniform rectangular grid. Dirichlet boundary conditions are enforced on each metal gate and homogeneous Neumann conditions on the rest of the domain boundary.

Electron and hole concentrations are obtained in different ways depending on the degree of quantum confinement. In all cases, we adopt the effective-mass approximation that has been demonstrated to be rather accurate for the structure dimensions and in the energy range considered in this article.[16]

In regions where quantum confinement is very weak, a semiclassical density of states (DOS), with the Fermi–Dirac occupation factor, is used. In regions where the quantum confinement is strong in two directions, the density of states is computed by solving the two-dimensional (2D) Schrödinger equation. Finally, in regions where quantum confinement is significant only in one direction, the DOS is written as a sum of 2D subbands that are obtained by solving the one-dimensional (1D) Schrödinger equation in the direction of confinement for each mesh point in the perpendicular direction.

For $Si_{1-x}Ge_x$-based devices, with $x<0.85$, electrons occupy states around the silicon six degenerate CB minima, two in each direction k_x, k_y, and k_z of the wave vector space. Each minimum of the CB is characterized by three different effective masses in the three directions, and hence the Schrödinger equation must be solved three times (see Fig. 1). The case $x>0.85$, in which electrons in the CB occupy states close to eight equivalent minima in the $\langle 111\rangle$ direction, is not considered here.

In the following, we discuss in some detail the expressions used for the carrier density as a function of the degree of quantum confinement considered.

A. Two-dimensional quantum confinement: One-dimensional electron or hole gas (1DEG-1DHG)

The 2D single-particle Schrödinger equation for electrons, given a CB profile $E_c(x,y)$, reads

$$-\frac{\hbar^2}{2}\nabla\cdot[(m^{k_\alpha})^{-1}\nabla\Psi_i^{k_\alpha}]+E_c(x,y)\Psi_i^{k_\alpha}=E_i^{k_\alpha}\Psi_i^{k_\alpha}, \tag{2}$$

where $\hbar=h/2\pi$, $\Psi_i^{k_\alpha}(x,y)$ represents the ith eigenfunction, $E_i^{k_\alpha}$ is the ith eigenenergy, m^{k_α} is the electron effective-mass tensor in the plane perpendicular to the direction of propagation,

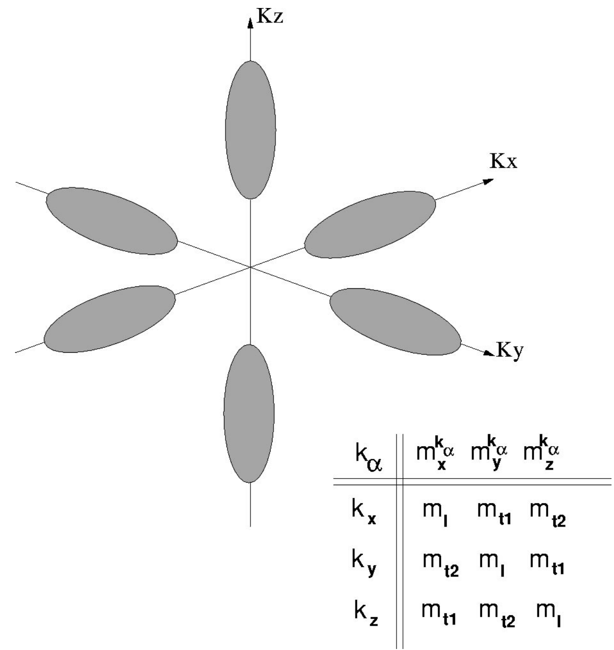

k_α	$m_x^{k_\alpha}$	$m_y^{k_\alpha}$	$m_z^{k_\alpha}$
k_x	m_l	m_{t1}	m_{t2}
k_y	m_{t2}	m_l	m_{t1}
k_z	m_{t1}	m_{t2}	m_l

FIG. 1. Six equivalent CB minima in the case of silicon and corresponding parameters of the effective-mass tensor.

$$m^{k_\alpha}=\begin{bmatrix} m_x^{k_\alpha} & 0 \\ 0 & m_y^{k_\alpha}\end{bmatrix}, \tag{3}$$

and k_α, with $\alpha=x$, y, z, identifies the axis of the wave vector space in which the CB minimum is placed. The coefficients of the electron effective-mass tensor are shown in Fig. 1, and the procedure for obtaining their value is described in the Appendix. In our simulations, we have discarded the exchange-correlation term, since it provides a very small contribution. Dirichlet boundary conditions are enforced on the quantum simulation domain, and the eigenvalue problem is solved according to a method described in Ref. 17.

The local DOS per unit volume and energy near a CB minimum is given by

$$N_{1D}(E,x,y)=\frac{\sqrt{2m_z^{k_\alpha}}}{\pi\hbar}\sum_i |\Psi_i^{k_\alpha}(x,y)|^2(E-E_i^{k_\alpha})^{-1/2} \times u(E-E_i^{k_\alpha}), \tag{4}$$

where $\alpha=x,y,z$ and $u(E-E_i^{k_\alpha})$ is the Heaviside function.

At this point, by integrating the DOS (4) multiplied by the Fermi–Dirac occupation factor on all CB minima, the quantum electron density can be expressed as

$$n=g_e\frac{\sqrt{2m_z^{k_x}k_BT}}{\pi\hbar}\sum_i |\Psi_i^{k_x}|^2F_{-1/2}\left(\frac{E_F-E_i^{k_x}}{k_BT}\right) +g_e\frac{\sqrt{2m_z^{k_y}k_BT}}{\pi\hbar}\sum_i |\Psi_i^{k_y}|^2F_{-1/2}\left(\frac{E_F-E_i^{k_y}}{k_BT}\right) +g_e\frac{\sqrt{2m_z^{k_z}k_BT}}{\pi\hbar}\sum_i |\Psi_i^{k_z}|^2F_{-1/2}\left(\frac{E_F-E_i^{k_z}}{k_BT}\right), \tag{5}$$

Downloaded 13 Jun 2007 to 131.114.53.157. Redistribution subject to AIP license or copyright, see http://jap.aip.org/jap/copyright.jsp

where g_e represents the degeneracy of each valley ($g_e=2$, in our case), $F_{-1/2}$ is the Fermi–Dirac integral of order $-1/2$, and E_F is the Fermi energy.

In order to compute the hole concentration, we have to solve the Schrödinger equation for heavy holes and for light holes. In this case, the CB in Eq. (2) is substituted by the inverted VB $-E_v(x,y)$, and the eigenvalues $-E_i^{hh}$ and $-E_i^{lh}$ for heavy or light holes, respectively, are obtained.

Therefore, we have

$$p=g_h\frac{\sqrt{2m_z^{lh}k_BT}}{\pi\hbar}\sum_i |\Psi_i^{lh}|^2F_{-1/2}\left(\frac{E_i^{lh}-E_F}{k_BT}\right)+g_h\frac{\sqrt{2m_z^{hh}k_BT}}{\pi\hbar}\sum_i |\Psi_i^{hh}|^2F_{-1/2}\left(\frac{E_i^{hh}-E_F}{k_BT}\right), \quad (6)$$

where g_h is valley degeneracy ($g_h=1$ in our case), and apices lh and hh refer to light and heavy holes, respectively.

B. One-dimensional quantum confinement: Two-dimensional electron or hole gas (2DEG-2DHG)

In the case of strong confinement in only one direction (e.g., along the x direction), we assume that the DOS can be decomposed in a quantum term along the confined direction (x) and a semiclassical term in the other directions. The 1D Schrödinger equation for electrons in the x direction for a mesh point y can be written as

$$-\frac{\hbar^2}{2m_x^{k_\alpha}}\frac{\partial^2}{\partial x^2}\Psi_i^{k_\alpha}+E_c(x,y)\Psi_i^{k_\alpha}=E_i^{k_\alpha}(y)\Psi_i^{k_\alpha}, \quad \alpha=x,y,z. \quad (7)$$

As a consequence, the available states for electrons are grouped into 2D subbands, and the DOS can be expressed as follows:

$$N_{2D}(E,x,y)=\frac{\sqrt{m_y^{k_\alpha}m_z^{k_\alpha}}}{2\pi\hbar^2}\sum_i |\Psi_i^{k_\alpha}(x,y)|^2u[E-E_i^{k_\alpha}(y)]. \quad (8)$$

By multiplying Eq. (8) by the Fermi–Dirac occupation factor and summing over the six minima, we obtain the electron density as

$$n=g_e\frac{k_BT\sqrt{m_y^{k_x}m_z^{k_x}}}{\pi\hbar^2}\sum_i |\Psi_i^{k_x}|^2\ln\left[1+\exp\left(\frac{E_F-E_i^{k_x}}{k_BT}\right)\right]+g_e\frac{k_BT\sqrt{m_y^{k_y}m_z^{k_y}}}{\pi\hbar^2}\sum_i |\Psi_i^{k_y}|^2\ln\left[1+\exp\left(\frac{E_F-E_i^{k_y}}{k_BT}\right)\right]+g_e\frac{k_BT\sqrt{m_y^{k_z}m_z^{k_z}}}{\pi\hbar^2}\sum_i |\Psi_i^{k_z}|^2\ln\left[1+\exp\left(\frac{E_F-E_i^{k_z}}{k_BT}\right)\right]. \quad (9)$$

Similar considerations apply to holes.

C. Effects of surface states

In the simulation of narrow QWs obtained with selective etching, the effects of states at the exposed surface are very important and must be taken into account in order to reproduce the experimental results with accuracy. In particular, for very narrow wires, such states can fully deplete the channel and completely screen the electric field imposed by external gates.

In order to correctly model surface states, we have used a simple model, based on two parameters, that is typically applied to metal–semiconductor contacts[15] and has been recently validated for air–semiconductor interfaces.[18] In particular, the two parameters are the density of interface states per unit energy per unit area D_S [$\mathrm{eV}^{-1}\,\mathrm{cm}^{-2}$], and the energy difference Φ^* between the vacuum level E_o and the Fermi energy that ensures a neutral charge at the interface. States with energy below $E_o-\Phi^*$ are donors and states with higher energy are acceptors.

Surface charge can then be expressed as

$$Q_s=-qD_S[E_F-(E_o-\Phi^*)].$$

D. Algorithm

The initial guess of the potential is obtained by solving the nonlinear Poisson equation with semiclassical approximation over the whole domain, with a Newton–Raphson (NR) iteration scheme. Afterwards, the Poisson–Schrödinger equation is solved with a NR algorithm that implements a simplified version of a predictor-corrector scheme[19] to accelerate convergence. Eigenfunctions and eigenvalues are computed only at the beginning of a NR cycle: for the whole cycle eigenfunctions and the difference between the eigenvalues and the energy bands in each point of the domain are assumed to be constant. This approach allows us to avoid solving the Schrödinger equation at each NR step, and is implemented by simply substituting the term E_i^* in Eqs. (5), (6), and (9), with $E_i^*-q(\Phi-\Phi^{prev})$, where Φ^{prev} is the potential used for the solution of the Schrödinger equation.

When a NR cycle ends, the Schrödinger equation is solved again and a new cycle is started. The program ends when the two-norm of the difference between the potential at the end of two successive NR cycles is lower then a fixed tolerance.[20]

This approach allows us to solve the eigenvalue problem only three or four times per simulation, while a single NR cycle is typically completed in seven to eight steps.

III. CONSIDERED STRUCTURES

Simulations have been performed on two different types of QWs obtained by selective etching on a modulation-doped SiGe-Si heterostructure: a single QW covered by a metal gate (Fig. 2) and a side-gated QW (Fig. 3).

The layer structure is the same for the two cases, and consists of a $Si_{0.8}Ge_{0.2}$ virtual substrate, an 11 nm SS layer in which the 1DEG and the 2DEG form, a 5.7 nm undoped $Si_{0.8}Ge_{0.2}$ spacer layer, a 5.7 nm $Si_{0.8}Ge_{0.2}$ doped layer, with $N_d=10^{18}\,\mathrm{cm}^{-3}$, a 35 nm undoped $Si_{0.8}Ge_{0.2}$ spacer and a 15 nm undoped silicon cap layer. The second spacer is rather thick, in order to prevent the formation of another electron channel in the silicon cap layer.

Quantum confinement of carriers in the horizontal (y) direction is provided by selective etching and by the deple-

Downloaded 13 Jun 2007 to 131.114.53.157. Redistribution subject to AIP license or copyright, see http://jap.aip.org/jap/copyright.jsp

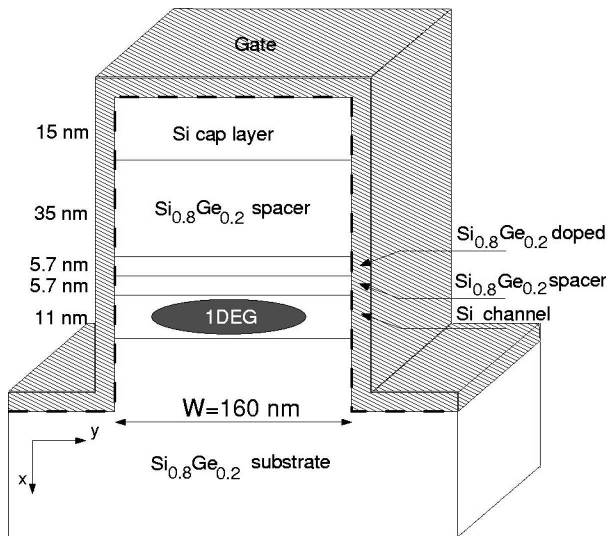

FIG. 2. Structure of the etched SSQW with triple metal gate structure considered in the simulations. Two-dimensional confinement is assumed in the SS layer.

tion region induced by acceptor states at the exposed surfaces, making the electrical width of wire significantly smaller then the etched width. Along the growth (x) direction, as a consequence of the band alignment between SS and silicon germanium, a quantum well for electrons forms. In particular, the tensile strain in the silicon layer lifts the degeneracy of CB minima, so that only the two lowest CB valleys along k_x are occupied and the energy splitting between valleys ($\approx$120 meV) is responsible for a strong suppression of intervalley scattering.

In the first structure, we assume that a triple metal gate is deposited over the structure forming a Schottky contact (Fig. 2). For the purpose of our simulation, the Schottky junction is reverse biased and assumed to be perfectly insulating. Results on this structure represent for us the upper limit of efficiency of the triple gate as far as electrical control of the wire is concerned (achievable with an extremely thin dielectric). We consider wires with etched width ranging from 20 to 200 nm, and assume a uniform density of interface states.

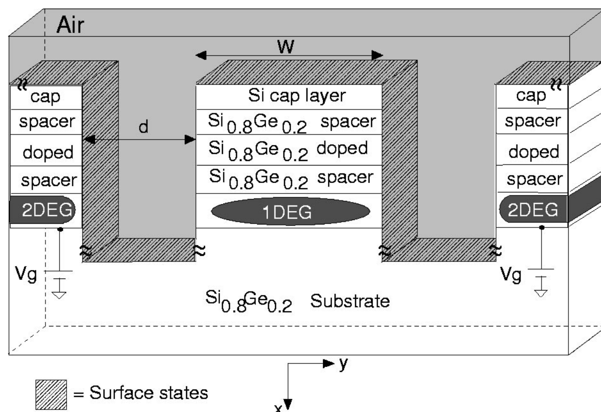

FIG. 3. Structure of the side-gated SSQW considered in the simulations. Two-dimensional confinement is assumed in the SS region in the wire, and 1D confinement in the SS layers used as side gates.

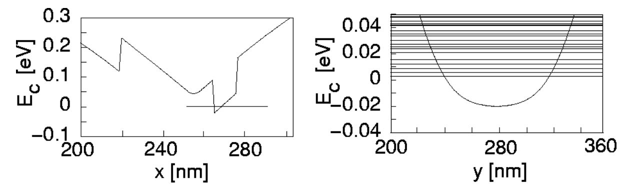

FIG. 4. CB profile in a 160-nm-wide SSQW, in the vertical direction (left) and in the horizontal direction (right).

In the second structure, shown in Fig. 3, we consider a side-gated structure. The QW has a width of 50 nm and is controlled via two side gates, realized with the same heterostructure, separated on both sides by an air gap of 30 nm. In this case, the capability to drive the electrical properties of wire via the gate voltage is very poor. As in the previous case, we assume a uniform DOS at the exposed surfaces of both the wire and the side gates.

We have studied the electron density and the conductance of the two structures as a function of the gate voltage and of D_S. Quantum confinement is only assumed in the SS regions, and is in two dimensions in the QW, and in one dimension in the SS regions used as side gates, as shown in Figs. 2 and 3.

IV. RESULTS AND DISCUSSION

In Fig. 4, we show the CB profile in two directions for a wire width $W = 160$ nm. The type of confinement is rather different in the two directions: in the vertical direction, the confinement is due of a very narrow triangular potential induced by modulation doping and heterointerfaces; in the horizontal direction, it is due to a very smooth quasiparabolic potential induced by the depletion regions near the exposed surfaces. Near the center of the wire, the horizontal potential is almost flat, due to the screening of the 1DEG.

This is also reflected in Fig. 5, where the difference between the ith and the first eigenvalue is plotted as a function of the waveguide width W.

As can be seen, for a width larger than 100 nm, eigenvalues are roughly equally separated, because of the quasi-

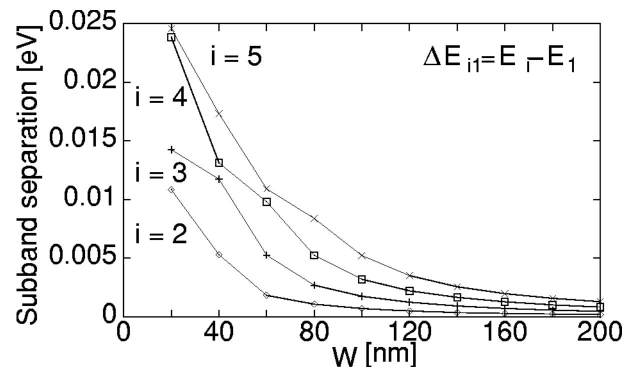

FIG. 5. Energy separation of 1D subbands as a function of wire width. E_i represents the ith eigenvalue energy. In waveguides wider than 100 nm, a quasiparabolic potential provides almost equally separated eigenvalues. The separation between adjacent modes is not uniform for narrower wires, as confinement in the x and y directions starts to be comparable, and eigenfunction nodes add also in the growth direction.

Downloaded 13 Jun 2007 to 131.114.53.157. Redistribution subject to AIP license or copyright, see http://jap.aip.org/jap/copyright.jsp

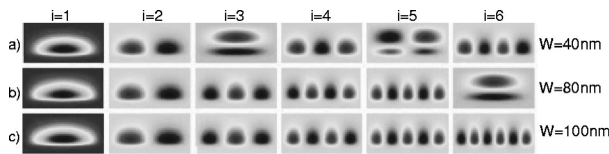

FIG. 6. Color map of the first six propagating modes in the SS waveguide for widths W=40, 80, and 100 nm. As the waveguide width is increased, nodes of the transversal eigenfunctions develop only in the lateral direction.

parabolic shape of the potential in the in-plane direction. The color map of the eigenfunctions corresponding to the lowest six eigenvalues for $W=40$, 80, and 100 nm is shown in Fig. 6. In the 100 nm case, additional nodes and maxima develop only in the horizontal direction, where confinement is weaker.

Separation between adjacent modes is not uniform for narrower wires, as confinement in the x and y directions starts to be comparable, and eigenfunction nodes add also in the growth direction, as can be seen in Fig. 6 for $W=80$ nm and $i=6$, and for $W=40$ nm and $i=3$ and 5.

For example, in Fig. 5, the separation between the third and the fourth eigenvalues for $W=40$ nm is very small. This is due to the fact that for $W>40$ nm, the third eigenfunction has two nodes in the horizontal direction (as shown in Fig. 6), and for $W=40$ nm, the third eigenfunction has one node in the horizontal direction and one node in the vertical direction.

Analogously, moving from wider to narrower wires, every alteration to the quasi-uniform energy spacing of propagating modes corresponds to a change of the configuration of nodes in the transversal wave function.

We would like to point out that the maximum separation between subband energies is obviously obtained for the narrowest wire considered (20 nm), and is 11 meV. Such a value is still smaller than the thermal energy at room temperature (26 meV), and poses some doubts on the possibility to suppress phonon scattering between subbands, and therefore to significantly increase electron mobility, in strongly confined QWs.[21] Indeed, it is still possible to increase the subband spacing somewhat, by further reducing the wire width and the SS thickness. However, it is worth noticing that the 20 nm wire is already completely depleted at equilibrium, if reasonable assumptions are made on interface states: for narrower wires, this would introduce a trade-off between desired confinement and voltage to be applied to the triple gate to populate the channel.

The electron density per unit length in the channel, for the first structure, is shown in Fig. 7, as a function of the external applied voltage and for several wire widths. The interface state parameters are those typical for exposed silicon:[15] $D_S=2.7\times10^{13}\,\mathrm{eV}^{-1}\,\mathrm{cm}^{-2}$ and $\Phi^*=4.7$ eV. As can be seen, the capability to control the electron density in the wire via the external gate does not depend on the wire width, since it is due mainly to the two lateral depletion regions. The capacitance per unit length is 0.24 fF/μm. The rather large capacitance obtained is due mainly to the fact that the potential profile in the horizontal direction is rather rigid; that is, it changes very little with the applied voltage.

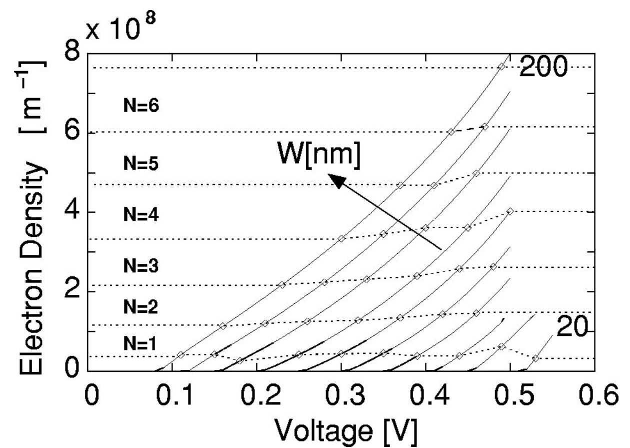

FIG. 7. Density of electrons per unit length in the channel as a function of the gate voltage, for the QW sketched in Fig. 2, for different wire widths, from 20 to 200 nm. Also shown is the number of propagating modes, that is, of modes with energy smaller than the Fermi level.

The number N of propagating modes (that is, of eigenvalues with energy smaller than the Fermi energy) is shown in the same graph. Excluding thermal averaging, the conductance is $G=N(4q^2/h)=NG_o$, where the conductance quantum G_o in silicon is twice the universal value due to valley degeneracy. From Fig. 7, it is also clear that the voltage required to add a propagating mode has a slight dependence on the wire width. Again, this is due to the fact that the transconductance is mainly controlled by the lateral depletion regions, that do not depend on the wire width.

The side-gated structure is much more sensitive to surface states, Indeed, values of D_S considered in the previous case, here would completely screen the field induced by the side gates. This is very clear once we realize that the capacitive coupling between the gates and the 1D channel is much weaker, and there are two air–semiconductor interfaces in between.

For this reason, in the simulation of the side-gated structure we consider a value of D_S two orders of magnitude smaller. A color plot of the distribution of the density of electrons is shown in Fig. 8 for an applied voltage of 0.5 V: electrons accumulate at the exposed surface of the side gates, and electron concentration in the QW is significantly smaller.

In Fig. 9, we show the electron density in the channel as a function of the voltage V_G applied to the side gates and D_S. It can be seen that in this case, for all values of D_S considered, the gate-to-channel capacitance is at least an order of magnitude smaller, due to the much larger distance between the gates and the wire.

In the same figure, the number of propagating modes, and therefore the conductance of the wire, is also shown. It should be noticed that, while the threshold voltage has a significant dependence on the value of D_S, the capacitance and the voltage required to add a propagating mode depend only smoothly on D_S, meaning that the range of D_S considered ensures that the external field is not screened at the surface.

Downloaded 13 Jun 2007 to 131.114.53.157. Redistribution subject to AIP license or copyright, see http://jap.aip.org/jap/copyright.jsp

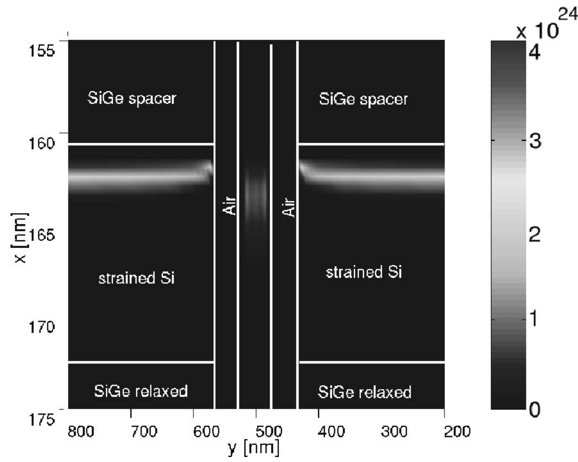

FIG. 8. Color map of the electron density in the side-gated structure illustrated in Fig. 3. White contours represent the geometry of the QW and of the side gates.

V. CONCLUSION

We have investigated quantum confinement and electrical properties in strained-silicon quantum wires controlled by external gates.

We have shown that both in a triple-gate structure and in a side-gated structure, the capability of controlling wire conductance via the gate voltage depends only weakly on the wire width since it is due mainly to the lateral two depletion regions. In particular, the side-gated heterostructure is much more sensitive to the effects of interface states that can completely screen the external field induced by the side gates.

The considered structures are very promising for obtaining large subband separation and hence suppression of phonon scattering in order to achieve low-temperature conductance quantization even in long wires. On the other hand, large mobility enhancement at room temperature, as predicted by Sakaki, is hardly achievable in these structures, since the typical subband separation is still smaller than thermal energy.

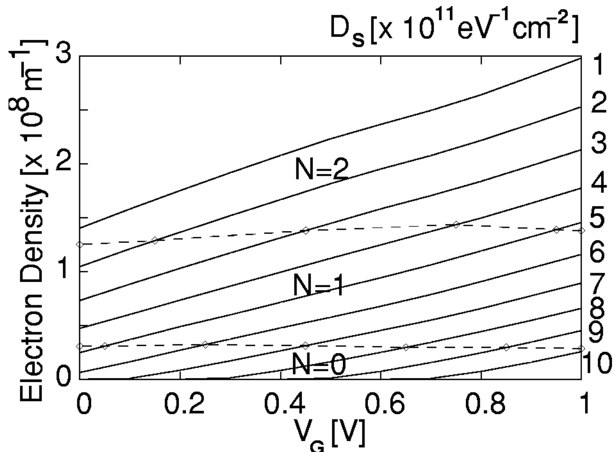

FIG. 9. Density of electrons per unit length in the QW illustrated in Fig. 3, as a function of the side-gate voltage, for a DOS at the exposed surface varying from 1×10^{11} to 10×10^{11} eV^{-1} cm^{-2}. The number N represent the number of occupied subbands as a function of the width, of the applied voltage and of the interface DOS.

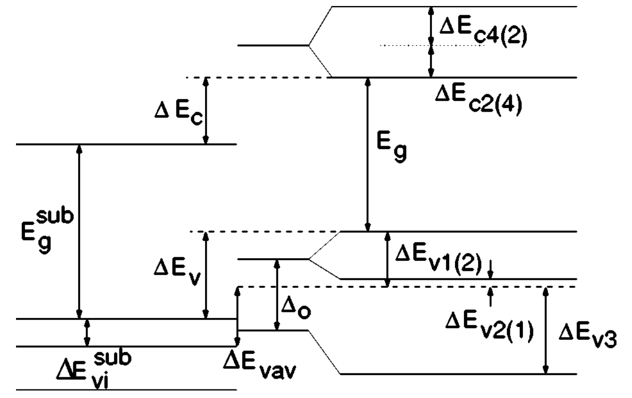

FIG. 10. Band alignment at the $Si_\alpha Ge_{1-\alpha}/Si_\beta Ge_{1-\beta}$ interface.

ACKNOWLEDGMENTS

This work has been supported by the European Union through the IST Project NANOTCAD (Nanotechnology Computer Aided Design), IST-1999-10828, and by the Italian Ministry of Education, University and Research through the PRIN project "Single Electron Devices." One author (G.I.) would like to thank F. Evangelisti and E. Giovine for the fruitful discussions.

APPENDIX: BAND PARAMETERS IN STRAINED $SI_\alpha GE_{1-\alpha}$ ALLOYS ON $SI_\beta GE_{1-\beta}$ SUBSTRATES

Here, we describe the procedure used for computing the band alignment at the $Si_\alpha Ge_{1-\alpha}/Si_\beta Ge_{1-\beta}$ interface. In Fig. 10, we schematically represent a strained layer grown onto a relaxed substrate and emphasize the strain-induced splitting of the CB minima and VB edges. It is important to notice that the procedure implemented is still valid even if the substrate is itself strained and the lattice constant is imposed by a third unstrained layer, but it fails if the germanium mole fraction in the substrate or in the epitaxial layer increases above 0.85.

The lattice constant in the substrate, as a function of germanium concentration, can be expressed as[22]

$$a_o(\beta)=a_o(\mathrm{Si})+0.200326\alpha(1-\beta)+[\mathrm{a_o(Ge)}-\mathrm{a_o(Si)}]\beta^2. \tag{A1}$$

The epitaxial layer lattice constant $a_\perp$ in the growth direction is given by[22]

$$a_\perp(\alpha)=a_o(\alpha)\left[1-2\frac{c_{12}(\alpha)}{c_{11}(\alpha)}\frac{a_\parallel(\alpha)-a_o(\alpha)}{a_o(\alpha)}\right], \tag{A2}$$

where c_{11} and c_{12} are the elastic constants.

Starting from the difference ΔE_{vav} between the weighted averages of VB edges at the Γ, we have computed the splitting from the average VB edge of the three VB edges ΔE_{v1}, ΔE_{v2}, ΔE_{v3} as a function of α and β:[22,23]

$$\Delta Ev_{\mathrm{av}}=(0.047-0.06\beta)(\alpha-\beta), \tag{A3}$$

$$\Delta E_{v2}=\tfrac{1}{3}\Delta_o-\tfrac{1}{2}\delta E_{001}, \tag{A4}$$

$$\Delta E_{v1}=-\tfrac{1}{6}\Delta_o+\tfrac{1}{4}\delta E_{001}+\tfrac{1}{2}[(\Delta_o)^2+\Delta_o\delta E_{001}+\tfrac{9}{4}(\delta E_{001})^2]^{1/2}, \tag{A5}$$

Downloaded 13 Jun 2007 to 131.114.53.157. Redistribution subject to AIP license or copyright, see http://jap.aip.org/jap/copyright.jsp

$$\Delta E_{v3} = -\tfrac{1}{6}\Delta_o + \tfrac{1}{4}\delta E_{001} - \tfrac{1}{2}[(\Delta_o)^2 + \Delta_o \delta E_{001} + \tfrac{9}{4}(\delta E_{001})^2]^{1/2}, \quad (A6)$$

where Δ_o is the experimental spin–orbit splitting in the unstrained material, and δE_{001} is the linear splitting of the multiplet.[23]

Similarly, the splitting of the twofold and fourfold CB minima with respect to the average CB edge can be expressed as follows:[22,23]

$$\Delta E_{c2} = \tfrac{2}{3}E_u(\epsilon_{zz} - \epsilon_{xx}), \quad (A7)$$

$$\Delta E_{c4} = -\tfrac{1}{3}E_u(\epsilon_{zz} - \epsilon_{xx}), \quad (A8)$$

where ϵ_{ii}, with $i = x, y, z$, are the components of the symmetric strain tensor, and E_u is a deformation potential. Hence, we can calculate the discontinuity between the VB edges, the gap in the strained layer, and finally the discontinuity between the CB minima:

$$\Delta E_v = \Delta E_{\mathrm{vav}} - \Delta E_{\mathrm{vi}}^{\mathrm{sub}} + \Delta E_{\mathrm{vi}}, \quad (A9)$$

where $\Delta E_{\mathrm{vi}}^{\mathrm{sub}}$ and ΔE_{vi} represent the difference between the maximum and the average VB edge in the substrate and in the epitaxial layer, respectively. $i = 1(2)$ in the case of tensile (compressive) strain. We have

$$E_g = E_g^{\mathrm{relax}} + \Delta E_{ci} - \Delta E_{vj} + \Delta E_{go} - \frac{\Delta_o}{3}, \quad (A10)$$

where ΔE_{go} is the gap variation as a consequence of an uniaxial strain in the growth direction,[24] and $j = 2, 4$ in the case of tensile or compressive strain, respectively. E_g^{relax} is the value of the energy gap known for the unstrained layer, which we take from Ref. 24. Finally,

$$\Delta E_c = E_g + \Delta E_v - E_g^{\mathrm{sub}}. \quad (A11)$$

The electron effective masses are calculated as a function of α and β,[22] while we have used for holes the values known for silicon. In particular, electron effective masses are calculated in the following way:

$$m_s(\alpha,\beta) = [1,(\alpha-\beta),(\alpha-\beta)^2]\cdot \mathbf{W} \cdot \begin{bmatrix} 1 \\ (\alpha+\beta) \end{bmatrix}, \quad (A12)$$

where $s = l, t1, t2$ identifies the longitudinal and transverse mass, and $\mathbf{W}$ is a 3×2 matrix.[22] Hole effective masses are computed as a function of Ge mole fraction in the strained layer and in the virtual substrate, following Ref. 25.

[1] K. Ismail, S. F. Nelson, J. O. Chu, and B. S. Meyerson, Appl. Phys. Lett. **63**, 660 (1993).
[2] N. Sugii, K. Nagakawa, Y. Kimura, S. Yamaguchi, and M. Miyao, Semicond. Sci. Technol. **13**, A140 (1998).
[3] J. L. Hoyt, H. M. Nayfeh, S. Eguchi, I. Aberg, G. Xia, T. Drake, E. A. Fitzgerald, and D. A. Antoniadis, Tech. Dig. - Int. Electron Devices Meet. **2002**, 23.
[4] U. Wieser, U. Kunze, K. Ismail, and J. O. Chu, Appl. Phys. Lett. **81**, 1726 (2002).
[5] A. Kristensen, J. B. Jensen, M. Zaffalon, C. B. Srensen, S. M. Reimann, P. E. Lindelof, M. Michel, and A. Forchel, J. Appl. Phys. **83**, 607 (1998).
[6] L. Worschech, F. Beuscher, and A. Forchel, Appl. Phys. Lett. **75**, 578 (1999).
[7] A. Yacoby, H. L. Stormer, N. S. Wingreen, L. N. Pfeiffer, K. W. Baldwin, and K. W. West, Phys. Rev. Lett. **77**, 4612 (1996).
[8] L. Worschech, B. Weidner, S. Reitzenstein, and A. Forchel, Appl. Phys. Lett. **78**, 3325 (2001).
[9] J. P. Colinge, X. Baie, V. Bayot, and E. Grivei, Solid-State Electron. **39**, 49 (1996).
[10] X. Huang, W.-C. Lee, C. Kuo, D. Hisamoto, L. Chang, J. Kedzierski, E. Anderson, H. Takeuchi, Y.-K. Choi, K. Asano, V. Subramanian, T.-J. King, J. Bokor, and C. Hu, IEEE Trans. Electron Devices **48**, 880 (2001).
[11] Y.-K. Choi, T.-J. King, and C. Hu, IEEE Trans. Electron Devices **49**, 436 (2002).
[12] M. Holzmann, D. Többen, G. Abstreiter, M. Wendel, H. Lorenz, and J. P. Kotthaus, Appl. Phys. Lett. **66**, 833 (1995).
[13] E. Giovine, A. Notargiacomo, L. Di Gaspare, E. Palange, F. Evangelisti, R. Leoni, G. Castellano, G. Torrioli, and V. Foglietti, Nanotechnology **12**, 132 (2001).
[14] R. A. Smith and H. Ahmed, J. Appl. Phys. **81**, 2699 (1997).
[15] S. M. Sze (Wiley, New York, 1981).
[16] F. Sacconi, M. Povolotskyi, A. Di Carlo, P. Lugli, M. Stadele, C. G. Strahberger, and P. Vogl, Physica B **314**, 345 (2002).
[17] M. G. Pala and G. Iannaccone, Nanotechnology **13**, 369 (2002).
[18] M. G. Pala, G. Iannaccone, S. Kaiser, A. Schliemann, L. Worschech, and A. Forchel, Nanotechnology **13**, 373 (2002).
[19] A. Trellakis and T. J. Galick, J. Appl. Phys. **81**, 7880 (1997).
[20] A. Trellakis and U. Ravaioli, J. Appl. Phys. **86**, 3911 (1999).
[21] H. Sakaki, Jpn. J. Appl. Phys. **19**, L735 (1980).
[22] M. Rieger and P. Vogl, Phys. Rev. B **48**, 14276 (1993).
[23] C. G. Van de Walle, Phys. Rev. B **34**, 5621 (1986).
[24] R. People and J. C. Bean, Appl. Phys. Lett. **48**, 538 (1986).
[25] S. K. Chun and K. L. Wang, IEEE Trans. Electron Devices **39**, 2152 (1992).

Downloaded 13 Jun 2007 to 131.114.53.157. Redistribution subject to AIP license or copyright, see http://jap.aip.org/jap/copyright.jsp